The Astrophysical Journal Letters, 944:L16 (12pp), 2023 February 20 https://doi.org/10.3847/2041-8213/acac92

PHANGS–JWST First Results: Destruction of the PAH Molecules in H II Regions Probed by JWST and MUSE

Oleg V. Egorov[1], Kathryn Kreckel[1], Karin M. Sandstrom[2], Adam K. Leroy[3], Simon C. O. Glover[4], Brent Groves[5], J. M. Diederik Kruijssen[6], Ashley. T. Barnes[7], Francesco Belfiore[8], F. Bigiel[7], Guillermo A. Blanc[9,10], Médéric Boquien[11], Yixian Cao[12], Jérémy Chastenet[13], Mélanie Chevance[4,6], Enrico Congiu[10], Daniel A. Dale[14], Eric Emsellem[15,16], Kathryn Grasha[17], Ralf S. Klessen[4,18], Kirsten L. Larson[19], Daizhong Liu[12], Eric J. Murphy[20], Hsi-An Pan[21], Ismael Pessa[22], Jérôme Pety[23,24], Erik Rosolowsky[25], Fabian Scheuermann[1], Eva Schinnerer[22], Jessica Sutter[2,26], David A. Thilker[27], Elizabeth J. Watkins[1], and Thomas G. Williams[22,28]

[1] Astronomisches Rechen-Institut, Zentrum für Astronomie der Universität Heidelberg, Mönchhofstraße 12–14, D-69120 Heidelberg, Germany
oleg.egorov@uni-heidelberg.de
[2] Center for Astrophysics & Space Sciences, Department of Physics, University of California, San Diego, 9500 Gilman Drive, San Diego, CA 92093, USA
[3] Department of Astronomy, The Ohio State University, 140 West 18th Avenue, Columbus, OH 43210, USA
[4] Universität Heidelberg, Zentrum für Astronomie, Institut für Theoretische Astrophysik, Albert-Ueberle-Str 2, D-69120 Heidelberg, Germany
[5] International Centre for Radio Astronomy Research, University of Western Australia, 35 Stirling Highway, Crawley, WA 6009, Australia
[6] Cosmic Origins Of Life (COOL) Research DAO[29]
[7] Argelander-Institut für Astronomie, Universität Bonn, Auf dem Hügel 71, D-53121 Bonn, Germany
[8] INAF—Osservatorio Astrofisico di Arcetri, Largo E. Fermi 5, I-50157, Florence, Italy
[9] Observatories of the Carnegie Institution for Science, 813 Santa Barbara Street, Pasadena, CA 91101, USA
[10] Departamento de Astronomía, Universidad de Chile, Camino del Observatorio 1515, Las Condes, Santiago, Chile
[11] Centro de Astronomía (CITEVA), Universidad de Antofagasta, Avenida Angamos 601, Antofagasta, Chile
[12] Max-Planck-Institut für extraterrestrische Physik, Giessenbachstraße 1, D-85748 Garching, Germany
[13] Sterrenkundig Observatorium, Universiteit Gent, Krijgslaan 281 S9, B-9000 Gent, Belgium
[14] Department of Physics and Astronomy, University of Wyoming, Laramie, WY 82071, USA
[15] European Southern Observatory, Karl-Schwarzschild Straße 2, D-85748 Garching bei München, Germany
[16] Univ Lyon, Univ Lyon 1, ENS de Lyon, CNRS, Centre de Recherche Astrophysique de Lyon UMR5574, F-69230 Saint-Genis-Laval, France
[17] Research School of Astronomy and Astrophysics, Australian National University, Canberra, ACT 2611, Australia
[18] Universität Heidelberg, Interdisziplinäres Zentrum für Wissenschaftliches Rechnen, Im Neuenheimer Feld 205, D-69120 Heidelberg, Germany
[19] AURA for the European Space Agency (ESA), Space Telescope Science Institute, 3700 San Martin Drive, Baltimore, MD 21218, USA
[20] National Radio Astronomy Observatory, 520 Edgemont Road, Charlottesville, VA 22903-2475, USA
[21] Department of Physics, Tamkang University, No. 151, Yingzhuan Road, Tamsui District, New Taipei City 251301, Taiwan
[22] Max-Planck-Institut für Astronomie, Königstuhl 17, D-69117, Heidelberg, Germany
[23] Institut de Radioastronomie Millimétrique (IRAM), 300 Rue de la Piscine, F-38406 Saint Martin d'Hères, France
[24] LERMA, Observatoire de Paris, PSL Research University, CNRS, Sorbonne Universités, F-75014 Paris, France
[25] Department of Physics, University of Alberta, Edmonton, AB T6G 2E1, Canada
[26] Leibniz-Institut für Astrophysik Potsdam (AIP), An der Sternwarte 16, D-14482 Potsdam, Germany
[27] Department of Physics and Astronomy, The Johns Hopkins University, Baltimore, MD 21218, USA
[28] Sub-department of Astrophysics, Department of Physics, University of Oxford, Keble Road, Oxford OX1 3RH, UK
Received 2022 October 20; revised 2022 December 7; accepted 2022 December 16; published 2023 February 16

Abstract

Polycyclic aromatic hydrocarbons (PAHs) play a critical role in the reprocessing of stellar radiation and balancing the heating and cooling processes in the interstellar medium but appear to be destroyed in H II regions. However, the mechanisms driving their destruction are still not completely understood. Using PHANGS–JWST and PHANGS–MUSE observations, we investigate how the PAH fraction changes in about 1500 H II regions across four nearby star-forming galaxies (NGC 628, NGC 1365, NGC 7496, and IC 5332). We find a strong anticorrelation between the PAH fraction and the ionization parameter (the ratio between the ionizing photon flux and the hydrogen density) of H II regions. This relation becomes steeper for more luminous H II regions. The metallicity of H II regions has only a minor impact on these results in our galaxy sample. We find that the PAH fraction decreases with the Hα equivalent width—a proxy for the age of the H II regions—although this trend is much weaker than the one identified using the ionization parameter. Our results are consistent with a scenario where hydrogen-ionizing UV radiation is the dominant source of PAH destruction in star-forming regions.

Unified Astronomy Thesaurus concepts: Polycyclic aromatic hydrocarbons (1280); H II regions (694); Interstellar dust (836)

1. Introduction

Polycyclic aromatic hydrocarbons (PAHs) are carbon-based macromolecules that are ubiquitous in the interstellar medium (ISM) and traced by several strong emission features at 3.3, 6.2, 7.7, 8.6, 11.3, 12.7, and 17 μm (Tielens 2008; Li 2020). Together with very small (20–30 Å) dust grains that have been stochastically heated, PAHs can be a dominant contributor to

[29] coolresearch.io

the mid-infrared (mid-IR) spectra of galaxies (e.g., Draine & Li 2007). The IR emission from PAHs is produced by the absorption and reemission of ultraviolet (UV) photons, with PAHs reprocessing as much as 20% of all stellar UV radiation (Smith et al. 2007). Because of this, they have been proposed as indicators of star formation rate (SFR; Calzetti 2013), but their usage for this purpose is complicated by our lack of understanding of the mechanisms for PAH formation and destruction (Whitcomb et al. 2020).

The PAHs are formed in the carbon-rich atmospheres of evolved stars (e.g., Latter 1991; Cherchneff et al. 1992), though these PAHs alone cannot account for all of the PAH emission observed in the ISM (e.g., Matsuura et al. 2009, 2013). The precursor molecules for PAHs have been found in dense clouds (Burkhardt et al. 2021), and high PAH fractions are observed in molecular clouds, which is difficult to explain if they do not form there given cloud lifetimes (Sandstrom et al. 2010; Chastenet et al. 2019). A popular scenario for PAH formation is the shattering of larger dust grains (e.g., Jones et al. 1996; Hirashita & Yan 2009; Seok et al. 2014; Wiebe et al. 2014). Both shocks and UV radiation play a critical but complex role in the evolution of PAHs. Shocks can increase the PAH fraction by dissociating large grains but also decrease the PAH abundance by destroying them directly (e.g., O'Halloran et al. 2006; Micelotta et al. 2010a). Similarly, UV radiation excites the IR bands in PAHs but can also destroy them (e.g., Allain et al. 1996; Pavlyuchenkov et al. 2013).

The PAH destruction is thought to be regulated by the radiation field, either by the high intensity of ionizing photons (Montillaud et al. 2013) or the hardness[30] of the radiation (Madden et al. 2006; Gordon et al. 2008). Theoretical works also suggest that PAHs are subject to sputtering and fragmentation in ionized gas due to electronic and atomic interactions (Micelotta et al. 2010b; Bocchio et al. 2012). These processes should destroy PAH molecules and thus reduce their abundance in H II regions. Observationally, this has been seen as a lack of PAH emission in the interior of Galactic H II regions (e.g., Povich et al. 2007) and an anticorrelation between the PAH fraction and tracers of the hardness and/or intensity of the ionizing radiation on large (global) scales (e.g., Madden et al. 2006; Gordon et al. 2008; Hunt et al. 2010; Lebouteiller et al. 2011; Maragkoudakis et al. 2018). Hydrogen-ionizing radiation is often considered a natural explanation for the observed decrease of the PAH abundances in low-metallicity galaxies and star-forming complexes (e.g., Engelbracht et al. 2005, 2008; Madden et al. 2006; Khramtsova et al. 2013).

The properties of star-forming regions (e.g., age, metallicity, density) establish the balance between the PAH formation and destruction processes. Multiwavelength observations of H II regions, their stellar populations, and associated photodissociation regions (PDRs) are therefore key for understanding the evolution of PAHs in the ISM of galaxies, and high (<100 pc) physical resolutions are critical to spatially isolating local from global effects (see also Chastenet et al. 2023a). Until now, such observations were possible mainly in H II regions in our Galaxy (e.g., Povich et al. 2007; Binder & Povich 2018) or very nearby galaxies (e.g., Bolatto et al. 2007; Sandstrom et al. 2010; Lebouteiller et al. 2011; Wiebe et al. 2011; Chastenet et al. 2017; Maragkoudakis et al. 2018; Chastenet et al. 2019; Mallory et al. 2022), while most extragalactic studies were focused on integrated observations of entire galaxies or large star-forming complexes (e.g., Engelbracht et al. 2005; Madden et al. 2006; Gordon et al. 2008; Khramtsova et al. 2013, 2014; Maragkoudakis et al. 2018; Lin et al. 2020).

With the launch of the JWST, it is now possible to investigate individual H II regions and their immediate surroundings in significantly more distant galaxies than ever before, covering a more representative view of the physical conditions in the ISM. Combining new JWST data with the available high-resolution data in different wavelength ranges, we can now probe the evolution of the PAHs and other grains in connection with the star-forming H II regions.

In this letter, we explore the abundance of PAH molecules within the boundaries of H II regions at 28–64 pc resolution in four nearby star-forming galaxies observed with JWST as the first targets in the PHANGS–JWST treasury program (Lee et al. 2023). We use MIRI images as tracers of emission from PAHs and very small dust grains. We combine these data with optical spectroscopy obtained from the MUSE integral-field spectrograph (Bacon et al. 2010) on the Very Large Telescope (VLT) as part of the PHANGS–MUSE program (Emsellem et al. 2022). Based on these data sets, we investigate the relation between the PAH fraction and the properties of the H II regions that could potentially be regulating their destruction (or formation). We refer the reader to the accompanying paper by Chastenet et al. (2023a), where we analyze the PAH fraction on galaxy-wide scales.

This letter is organized as follows. In Section 2, we describe the underlying observational data. Section 3 provides details on the methods and criteria implemented for selection of the H II regions and deriving the properties of the gas, dust, and young stars there. Section 4 describes results from the comparison of our tracer for PAH abundance and properties of the H II regions. Section 5 summarizes our results.

Table 1
Properties of the Galaxies

Galaxy	D (Mpc)	$R_{25}^{\dagger}$ (kpc)	$\log M_{*}^{+}$ ($M_{\odot}$)	$\log(\mathrm{SFR})^{+}$ ($M_{\odot}$ yr^{-1})	12+log (O/H)* at $R_{\rm eff}$	$N_{\rm H\ II}$
IC 5332	9.01[1]	8.0	9.67	−0.39	8.30	208
NGC 628	9.84[1]	14.1	10.34	0.24	8.48	668
NGC 1365	19.57[1]	34.2	10.99	1.23	8.48	365
NGC 7496	18.72[2]	9.1	10.00	0.35	8.51	288

References: [†]Paturel et al. (2003); Shaya et al. (2017); Kourkchi et al. (2020); [1]Anand et al. (2021a, 2021b); [2]Anand et al. (2021a); [+]Leroy et al. (2021); [*]Groves et al. (2023).

2. Observations

2.1. Galaxy Sample

We analyze H II regions in the first four PHANGS–JWST galaxies. These galaxies have all been observed with VLT/MUSE and thus are ideal objects to relate the properties of ionized gas to the PAH emission. These nearby ($D \sim 9$–20 Mpc) galaxies span an order of magnitude in stellar mass (see Table 1) and almost 2 orders of magnitude in SFR. Two galaxies (NGC 1365 and NGC 7496) host active galactic nuclei

[30] Various definitions are used in the literature (e.g., the effective temperature or the spectral index of the UV spectrum). Here we define "hardness" as the ratio of the fluxes over hard and soft UV ranges (see Appendix A).

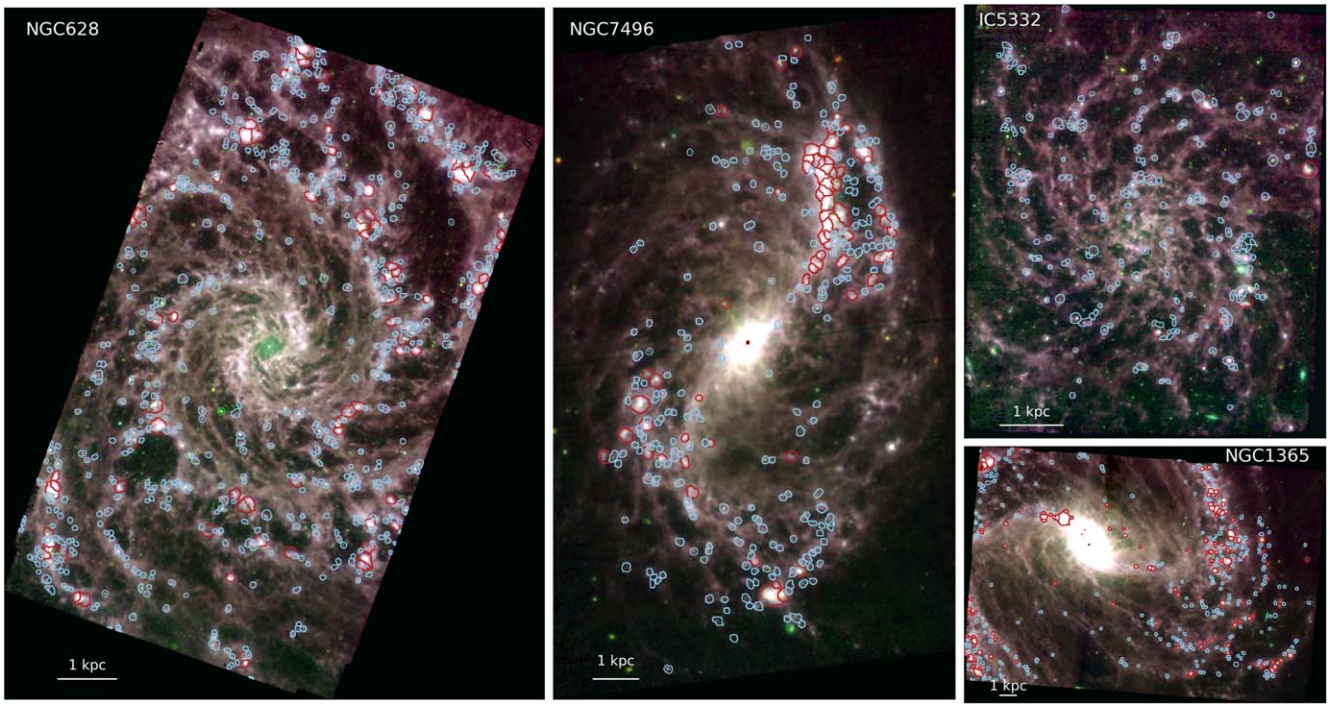

Figure 1. JWST/MIRI images in the F770W, F1000W, and F1130W bands (red, green, and blue channels, respectively) of the four galaxies analyzed in this letter. Contours show the borders of individual H II regions selected from MUSE data, which meet the criteria in Section 3.1. Blue contours correspond to the H II regions with a hydrogen-ionizing photon rate $Q^0 < 10^{50}$ s^{-1}, and red contours correspond to those with $Q^0 > 10^{50}$ s^{-1}.

(AGNs) and strong bars. Galaxy NGC 628 is a prototypical grand-design spiral, while IC 5332 shows a flocculent spiral morphology. They represent a good cross section of the PHANGS–JWST sample (Figure 1).

2.2. PHANGS–JWST

The JWST data were obtained in Cycle 1 as part of the PHANGS–JWST program (ID 02107; PI: J. C. Lee). The survey targets 19 nearby star-forming galaxies with NIRCam (F200W, F300M, F335M, and F360M) and MIRI (F770W, F1000W, F1130W, and F2100W) imaging. The first four galaxies have been observed, and their MIRI images (Figure 1) form the basis of our analysis. These galaxies have been imaged with two (for IC 5332 and NGC 7496), three (for NGC 628), or four (for NGC 1365) MIRI pointings (88.8, 122.1, 310.8, and 321.9 s per pointing in the F770W, F1000W, F1130W, and F2100W bands, respectively, and with four dithers per pointing to properly sample the point-spread function, PSF) covering an area well matched to the PHANGS–MUSE (Emsellem et al. 2022) and PHANGS–HST observations (Lee et al. 2022). The sensitivity of the data is similar for all four galaxies in all MIRI bands (0.11–0.15 MJy sr^{-1} at the 1σ level) except F2100W ($\sim$0.25 MJy sr^{-1}). We convolve all images to the PSF of the F2100W images (FWHM $\simeq$ 0.″67; corresponding to 28–64 pc at the distance of our targets), as obtained via the WEBBPSF (Perrin et al. 2014) model.[31] Convolution kernels were created following the procedure from Aniano et al. (2011). Standard calibrations are applied, with minor modifications. A detailed description of the complete data reduction is presented in Lee et al. (2023).

2.3. PHANGS–MUSE

All of the galaxies in the PHANGS–JWST program were previously observed with VLT/MUSE as part of the PHANGS–MUSE large program (PI: Schinnerer). The reduced data are publicly available,[32] and the details of the observations and data reduction are given in Emsellem et al. (2022). The angular resolution of the MUSE data for the objects in this study is $\sim$1″ (45–95 pc), sufficient to isolate individual H II regions from the surrounding diffuse ionized gas (DIG).

Based on MUSE Hα emission line maps, a catalog of $\sim$30,000 nebulae has been constructed (Santoro et al. 2022, Groves et al. 2023). The nebulae were selected using HIIPHOT (Thilker et al. 2000), which results in spatial masks that define the borders of each nebula. The catalog contains the derived properties of each nebula (e.g., emission line fluxes, velocity dispersion, equivalent width, and metallicity) based on their integrated spectra. The emission lines from each nebula are corrected for the effects of dust extinction using the Balmer decrement, as described in Groves et al. In the remainder of this paper, we use the extinction-corrected values. We do not correct the measured fluxes for the contribution of the DIG. The H II regions are selected from the nebula catalog based on the Baldwin et al. (1981) diagnostics considering [O III]/Hβ versus [N II]/Hα and [S II]/Hα line ratios, as described in Groves et al. (2023; see also Kewley et al. 2019 for a review). The present analysis is restricted to only those H II regions that meet stringent surface brightness and signal-to-noise ratio (S/N) criteria (see Section 3.1).

[31] https://webbpsf.readthedocs.io/en/stable/index.html

[32] https://archive.eso.org/scienceportal/home?data_collection=PHANGS

3. Deriving the Properties of the Ionized Gas and PAHs in Star-forming Regions

3.1. Selection of the Nebulae and Associated PAH Emission

We use the spatial masks from the PHANGS–MUSE nebular catalog (see Section 2.3) to identify the positions of H II regions in the JWST data. To do that, we reproject these masks to the JWST images. Since two of our galaxies contain an AGN, which produces hard ionizing radiation that can significantly affect the PAH fraction (e.g., Jensen et al. 2017; García-Bernete et al. 2022; Lai et al. 2022), we exclude the centers of the galaxies from our analysis. Masks that isolate these particular environments are taken from Querejeta et al. (2021).

In order to minimize the DIG contribution to the regions' flux, which could bias the derived properties of the nebulae, we select only those H II regions with a high Hα equivalent width EW(Hα) >16 Å and Hα surface brightness $\Sigma(\mathrm{H}\alpha) > 10^{39}$ erg s^{-1} kpc^{-2} (e.g., Belfiore et al. 2022). We also require S/N >5 in every emission line considered in this letter and S/N >15 in the Hα line. This ensures that we can recover accurate reddening-corrected fluxes of emission lines and derived properties for each of the nebulae.

In total, we select 1529 H II regions across all four galaxies ($N_{\mathrm{H\ II}}$ in Table 1), about 25% of the H II regions in our catalog (37% for NGC 1365). We derive the ratio log([S III]9069, 9532 Å/[S II]6717, 6731 Å),[33] which is a proxy for the ionization parameter (the ratio of the local ionizing photon flux and the local hydrogen density; Kewley & Dopita 2002), and we measure the oxygen abundance $12 + \log(\mathrm{O/H})$ (a proxy for gas-phase metallicity) with the S-calibration from Pilyugin & Grebel (2016). We integrate the fluxes in each JWST MIRI band within the apertures corresponding to the reprojected mask for each region. Some ratios of these mid-IR fluxes trace the PAH abundance in the ISM. We do not correct the measured fluxes for a possible contribution from the diffuse ISM. Note, however, that removing the local background measured in circular apertures around H II regions does not qualitatively affect the results presented below.

3.2. Tracing the PAH Fraction in the ISM

The ratio of total fluxes in the Spitzer bands $F_{8\mu\mathrm{m}}/F_{24\mu\mathrm{m}}$ is often considered as a tracer of q_{PAH}, the mass fraction of PAH molecules with respect to the total dust mass (e.g., Engelbracht et al. 2005; Bolatto et al. 2007; Sandstrom et al. 2010; Khramtsova et al. 2014; Oey et al. 2017). Sandstrom et al. (2010) showed that $F_{8\mu\mathrm{m}}/F_{24\mu\mathrm{m}}$ is indeed a good tracer of q_{PAH}, although it has a large scatter in the diffuse low-metallicity ISM where $q_{\mathrm{PAH}} < 1.5\%$. Khramtsova et al. (2013) found a stronger correlation between these parameters in star-forming regions.

In the case of JWST, the flux of the F2100W band traces the emission from very small dust grains (similar to Spitzer 24 μm) and correlates with the total IR luminosity (F_{TIR}), whereas F770W and F1130W are dominated by PAH features at 7.7 μm (similar to Spitzer 8 μm) and 11.3 μm, respectively, and trace the neutral and ionized ISM (Sandstrom et al. 2023). Models by Draine et al. (2021) show that q_{PAH} is proportional to both $F_{7.7}/F_{\mathrm{TIR}}$ and $F_{11.2}/F_{\mathrm{TIR}}$. Using $F_{2100\mathrm{W}}$ as a proxy for F_{TIR} introduces an unknown scaling but provides a robust empirical tracer of q_{PAH} (Chastenet et al. 2023a). In this letter, we consider both the 7.7 and 11.3 μm PAH features and assume that

$$q_{\mathrm{PAH}} \propto R_{\mathrm{PAH}} = \frac{F_{\mathrm{F770W}} + F_{\mathrm{F1130W}}}{F_{\mathrm{F2100W}}}. \quad (1)$$

Similarly to the works mentioned above, we further assume that R_{PAH} changes in H II regions mostly due to variations of the PAH fraction regulated by the processes of their formation and destruction. Note, however, that redistribution of the dust grains of different sizes can also affect R_{PAH} if the relative abundance of very small grains is changing in H II regions. For example, Everett & Churchwell (2010) hypothesized that the very small grains could be resupplied by the destruction of the dense embedded cloudlets overrun by the expansion of a bubble. Furthermore, radiation pressure–driven shift and/or the stellar winds (Gail & Sedlmayr 1979; Draine 2011) can redistribute the PAHs and very small grains, which has been suggested as a mechanism for evacuating the dust grains from the interior of several Galactic H II regions (Paladini et al. 2012). The shell-like morphology of the Galactic H II regions is indeed clearly seen in the mid-IR bands, especially in PAH-sensitive bands (e.g., Anderson et al. 2014). However, small grains (<100 Å) drift much more slowly than larger grains, and the difference between the PAHs and the very small grains is insignificant (Draine 2011). Thus, these processes should not significantly change the relative fraction of PAHs within the H II regions. Nevertheless, both of these effects can change the relative brightness of the rims of the H II regions in the mid-IR bands. Given that we analyze the ratios of the fluxes integrated over the H II regions, excluding the surrounding PDR (at least for the resolved H II regions; see Section 4.1), our results presented below are unlikely to be affected by these processes.

4. Results and Discussion

4.1. Destruction of PAHs by UV Radiation

The PAH destruction is expected to be correlated with the hardness and intensity of the radiation field (see Section 1). In previous works (e.g., Madden et al. 2006; Gordon et al. 2008; Lebouteiller et al. 2011; Maragkoudakis et al. 2018), the flux ratio of the neon IR lines [Ne III] 15.56/[Ne II] 12.81 μm was used as a tracer of the hardness of the ionizing radiation field. As shown in Kewley et al. (2019), this ratio is dependent on both the ionization parameter and the metallicity. In turn, the hardness of the radiation field depends on the metallicity (e.g., Groves et al. 2008) and can be correlated with the ionization parameter in H II regions (see discussion in Kumari et al. 2021). In this work, we use another tracer of the ionization parameter, [S III] λ9069, 9532/[S II] λ6717, 6731 Å, which can be measured in optical spectra. In contrast to [Ne III]/[Ne II], this ratio of sulfur lines is almost independent of metallicity (Kewley et al. 2019) and thus allows us to explore the relation of PAH abundances with the properties of the ionizing radiation field and the metallicity separately.

In Figures 2(a) and (b), we demonstrate how R_{PAH} depends on log([S III]/[S II]) in the 1529 H II regions. The data show a strong anticorrelation, implying that the PAH fraction in H II regions is tightly related to the ionization parameter. This

[33] While [S III] λ9532 is outside the MUSE spectral range, the two [S III] lines show a fixed ratio, which we assume to be [S III] λ9532Å $\simeq 2.5 \times$ [S III] λ9069 Å (Osterbrock & Ferland 2006).

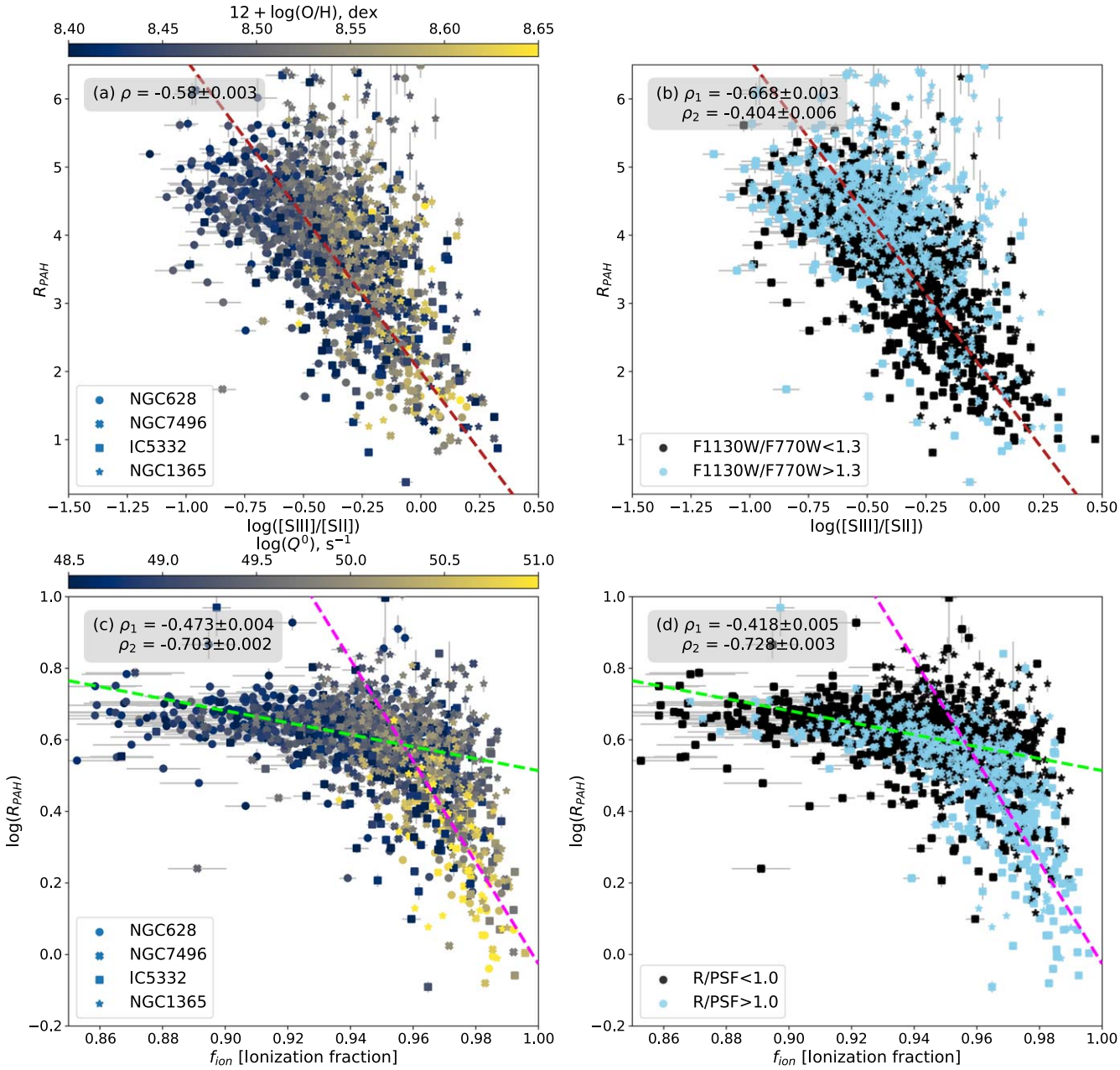

Figure 2. Correlation of PAH abundance, traced by $R_{\rm PAH}$, with ionization parameter, traced by log([S III]/[S II]) (panels (a) and (b)) or ionization fraction $f_{\rm ion}$ (panels (c) and (d)). Color encodes the oxygen abundance 12 + log(O/H) (panel (a)); ratio of F1130W/F770W, a proxy for the ionization state of PAHs (panel (b)); number of hydrogen-ionizing photons Q^0 (panel (c)); and effective radii of the H II regions relative to the PSF of the MUSE data (panel (d)). Dashed lines show a linear fit for the H II regions (Equation (2) for panels (a) and (b)). Faint ($Q^0 < 10^{50}$ s^{-1}; green dashed line, Equation (3)) and bright ($Q^0 > 10^{50}$ s^{-1}; magenta dashed line, Equation (4)) H II regions are considered separately in panels (c) and (d). Spearman's correlation coefficient (ρ) is given in the corner of each plot. Coefficients ρ_1 and ρ_2 are calculated separately for the black and cyan points (panels (b) and (d)) or faint and bright regions (panel (c)), respectively. The errors on ρ are derived from 1000 Monte Carlo realizations with the data randomly distributed around the measured values within the uncertainties.

anticorrelation can be parameterized linearly as

$$R_{\rm PAH} = (-4.58 \pm 0.16) \times \log([\mathrm{S\,III}]/[\mathrm{S\,II}]) + \\ + (1.99 \pm 0.06) + \Delta R_{\rm O/H}, \quad (2)$$

where $\Delta R_{\rm O/H}$ accounts for any secondary dependence on metallicity. For now, we assume $\Delta R_{\rm O/H} = 0$, as we do not see a significant secondary correlation of $R_{\rm PAH}$ with 12 + log(O/H) in panel (a) (but see Section 4.2).

Panel (b) of Figure 2 illustrates that the regions with higher $R_{\rm PAH}$ have, in general, a higher ratio of F1130W/F770W $\propto F_{11.3\mu\rm m}/F_{7.7\mu\rm m}$. This ratio is often used as a diagnostic of the neutral-to-ionized PAH ratio (e.g., Draine & Li 2001; Maragkoudakis et al. 2018). Neutral PAHs have a higher ratio of $F_{11.3\mu\rm m}/F_{7.7\mu\rm m}$, which decreases as the fraction of ionized PAHs increases. Thus, the distribution of F1130W/F770W shown in this plot is consistent with a scenario where the PAHs are ionized and destroyed in the H II regions with higher ionization parameters. Note, however, that this ratio can be affected by changes of the PAH size in higher intensity and harder radiation fields. The PAH feature at 3.3 μm, together with $F_{11.3\mu\rm m}/F_{7.7\mu\rm m}$, can help to disentangle the impact of PAH size from variations in the radiation field (Draine et al. 2021; Dale et al. 2023). We refer the reader to Chastenet et al. (2023b), who demonstrated that

PAHs are not only more ionized but also have smaller sizes in H II regions, which is consistent with their gradual destruction in such environments.

Panel (c) of Figure 2 provides some tentative conversions from the empirical correlations in panels (a) and (b) toward a more physical interpretation. It shows $\log(R_{\rm PAH})$ versus $f_{\rm ion}$, the ionization fraction of hydrogen in each H II region. The latter is calculated from log([S III]/[S II]) using the empirical parameterization from Kreckel et al. (2022). The color corresponds to the number of ionizing photons required to produce the observed Hα luminosity L(Hα): $Q^0 \simeq 7.33 \times 10^{11} L(\mathrm{H}\alpha)$ assuming $T_e = 10{,}000$ K (Osterbrock & Ferland 2006), with L(Hα) expressed in units of erg s^{-1}. In this representation, two different sequences are suggested when examining the dependence of the PAH fraction on $f_{\rm ion}$. Namely, $R_{\rm PAH}$ only slightly decreases with increasing $f_{\rm ion}$ (and ionization parameter) for fainter H II regions, even when the ionization fraction is high. In turn, bright regions (likely associated with more massive star clusters) more strongly affect the PAH fraction. We perform separate linear fits to the faint and bright H II regions (shown by green and magenta dashed lines in Figure 2(c), respectively):

$$\log(R_{\rm PAH})_{Q^0<10^{50}} = (-1.7 \pm 0.2) f_{\rm ion} + (2.2 \pm 0.2), \quad (3)$$

$$\log(R_{\rm PAH})_{Q^0>10^{50}} = (-14.2 \pm 1.4) f_{\rm ion} + (14.2 \pm 1.3). \quad (4)$$

Given the well-known size–luminosity relation for H II regions (e.g., Wisnioski et al. 2012), a probable explanation of the bimodality of the $\log(R_{\rm PAH})$ versus $f_{\rm ion}$ relation is a difference in their sizes. This difference can have either a physical or observational origin (or a combination). On the one hand, the larger, brighter regions might encompass the full scale height of the galactic disk and exhibit $q_{\rm PAH} \sim 0$ because the ISM is fully ionized toward these regions. On the other hand, the size of the regions that are unresolved with MUSE might be overestimated, while for well-resolved regions, the reprojected masks (see Section 3.1) should better isolate the H II regions. Thus, in the unresolved regions, one may expect to see a higher contribution from the diffuse ISM to the measurements. The effects leading to the redistribution of the dust grains at the outskirts of H II regions (mentioned in Section 3.2) may also be more prominent. Panel (d) of Figure 2 shows the same plot as panel (c), but all points are color-coded by R/PSF, their effective angular radius relative to the resolution (FWHM of PSF) of the MUSE data. The colored dashed lines show the regressions as in panel (c) defined by Equations (3) and (4). Indeed, we start to resolve the H II regions with MUSE at $Q^0 \sim 10^{50}$ s^{-1}, which naturally explains the bimodality. Future JWST observations of more nearby galaxies will help to clarify if the differences between the faint and bright H II regions are real or just an effect of the limited resolution. Note that excluding the unresolved regions with R/PSF < 1 (64% of our sample) from consideration in panels (a)–(c) of Figure 2 does not affect our results, but the resolved regions do demonstrate a much tighter correlation with log ([S III]/[S II]) (see Appendix B).

In our measurements, we do not attempt to correct for the contribution of the diffuse ISM to the optical emission line fluxes or mid-IR bands because performing a local background subtraction depends heavily on the exact H II region boundaries we define and potentially introduces large uncertainties into our measurements. Nevertheless, we validate in Appendix B that our results do not change if we keep only those regions where the background emission is negligible compared to our measured fluxes. From this, we conclude that unresolved regions and contamination by the DIG/background mid-IR emission do not change our results but are responsible for the scatter in Figure 2.

4.2. Dependence of the PAH Abundance on Metallicity

The dependence of the PAH abundance on metallicity has been explored for galaxy-wide scales and individual large star-forming complexes (e.g., Engelbracht et al. 2005; Khramtsova et al. 2013; Aniano et al. 2020). While $q_{\rm PAH}$ is clearly systematically lower in dwarf galaxies compared to spiral galaxies, in the high-metallicity regime, this relation exhibits a considerable scatter. The galaxies in our sample have relatively high metallicity and cover only 0.3 dex of dynamic range ($8.3 < 12 + \log(\mathrm{O/H}) < 8.6$), which could contribute to the lack of a clear secondary dependence of $R_{\rm PAH}$ with oxygen abundance in Figure 2(a).

To explore the secondary dependence of $R_{\rm PAH}$ with metallicity, we subtract the relation in Equation (2) from our measurements and correlate the residuals $\Delta R_{\rm PAH}$ with $12 + \log(\mathrm{O/H})$ in Figure 3(a). We find a mild correlation between these values only considering the 2D histogram representing the statistical density of the points on this plot. This correlation can be parameterized linearly as

$$\Delta R_{\rm O/H} = (11.3 \pm 0.5) \times ([12 + \log(\mathrm{O/H})] - 8.69) + (2.2 \pm 0.1). \quad (5)$$

Using this $\Delta R_{\rm O/H}$ in Equation (2), we can describe the PAH fraction in H II regions as a function of the characteristics of the ionized gas—its ionization parameter and metallicity. The dominant factor defining $R_{\rm PAH}$ is the ionization parameter, and the metallicity plays only a minor role leading to scatter in Figures 2(a) and (b). Note that we do not find any prominent secondary relation of the PAH fraction on other parameters (F1130W/F770W, Q^0) explored in Figure 2 (the bend in the trend for Q^0 in Figure 3(c) is probably due to the bimodality discussed in Section 4.1).

To demonstrate that we are not missing a primary correlation between $R_{\rm PAH}$ and metallicity, we show the 2D histogram distribution of these values in Figure 4(a). Red symbols in this panel correspond to the values averaged over all regions within each galaxy. These averaged values show an expected mild trend of increasing PAH fraction with the higher metallicity. At the same time, the distribution of the individual H II regions demonstrates the opposite trend: a very weak anticorrelation of $R_{\rm PAH}$ with oxygen abundance (similar to that for a small sample of high-metallicity galaxies in Engelbracht et al. 2008).

Overall, we conclude that the PAH destruction in H II regions is nearly independent of metallicity, at least for the range of oxygen abundances we consider. Analyzing highly resolved data for the LMC and SMC, Chastenet et al. (2019) also found a similar $q_{\rm PAH}$ in the luminous H II regions of those two galaxies, despite their difference in metallicity and a difference in their global $q_{\rm PAH}$ values. This supports our claim that the weakness of the metallicity dependence is not only due to the limited range of $12 + \log(\mathrm{O/H})$ in our data. At the same time, Chastenet et al. (2023a) found a much stronger correlation between $R_{\rm PAH}$ and the metallicity of the diffuse ISM, where the intensity of Hα is low. These results together imply that the metallicity regulates the PAH destruction and

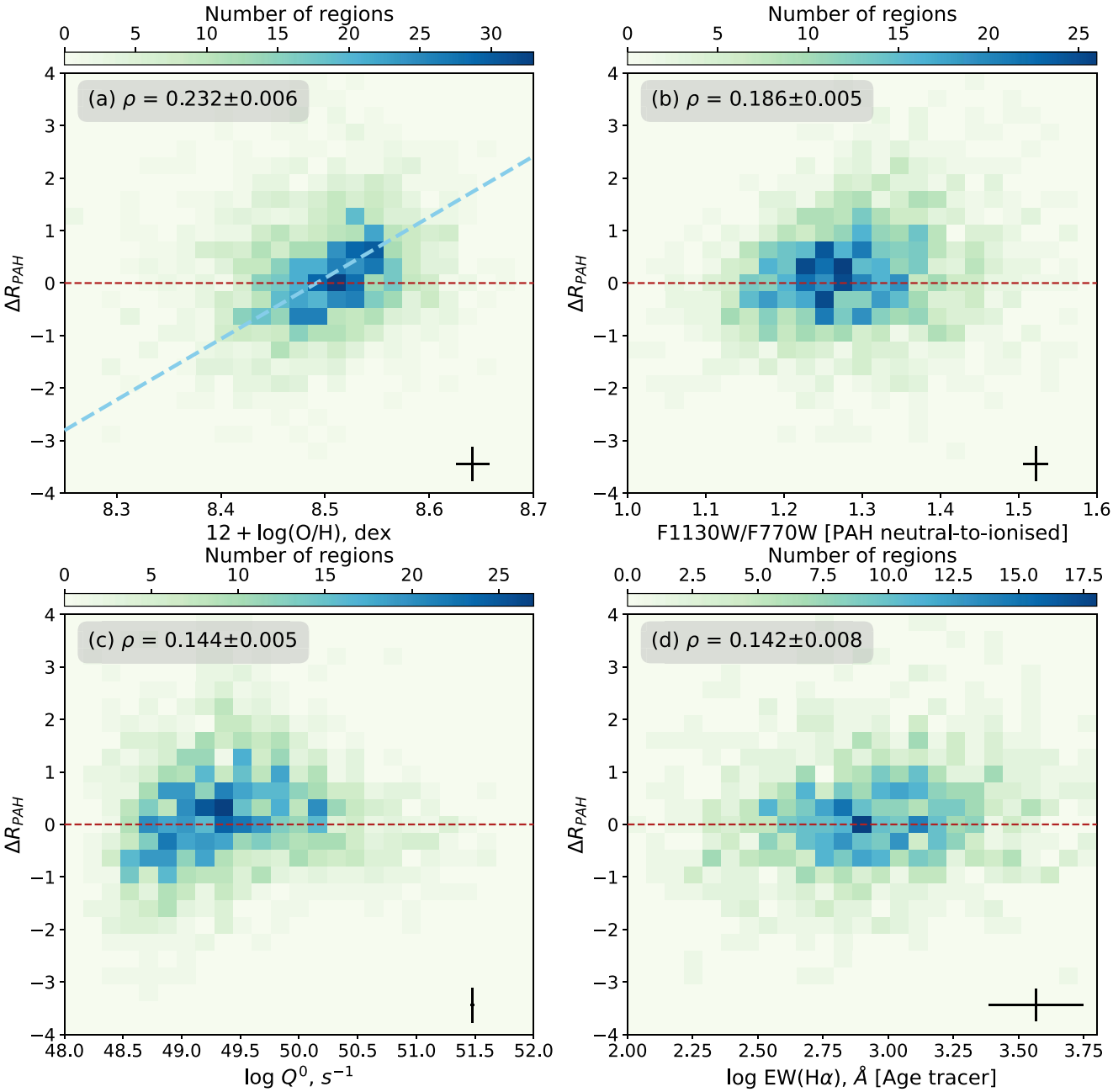

Figure 3. Secondary dependence of the PAH fraction on the oxygen abundance of H II regions, measured as 12 + log(O/H) (panel (a)); the F1130W/F770W flux ratio, sensitive to the relative fraction of neutral to ionized PAH (panel (b)); the number of hydrogen-ionizing photons Q^0 (panel (c)); and the equivalent width of Hα, corrected for the contribution of the underlying old stellar population (panel (d)). The 2D histograms in each panel show the distribution of $\Delta R_{\rm PAH}$, obtained after subtracting the values derived by Equation (2) from the measured $R_{\rm PAH}$. The red dashed line shows a zero-difference level. The light blue dashed line in panel (a) corresponds to a linear fit defined by Equation (5), tracing the secondary relation of $R_{\rm PAH}$ on metallicity. Spearman's correlation coefficient (ρ) is given in the corner of each plot. Its uncertainty is derived in the same way as in Figure 2. The error bars in the right-hand corner correspond to the 95th percentile uncertainties of the measured values.

formation processes, but it becomes much less important in the H II regions, where the presence of a large amount of ionized gas and intense ionizing radiation plays a dominant role.

4.3. The Role of UV Hardness

The PAH fraction in H II regions strongly correlates with the [S III]/[S II] line ratio, with only a mild secondary dependence on the metallicity. While [S III]/[S II] is a good tracer of the ionization parameter, it is also weakly dependent on the hardness of the UV radiation field (see Appendix A). Many previous studies found a correlation between the PAH fraction and the hardness of the radiation field at the scale of star-forming complexes (e.g., Madden et al. 2006; Gordon et al. 2008; Khramtsova et al. 2014; Maragkoudakis et al. 2018); thus, we cannot be sure that the trend seen in Figure 2 is driven by the intensity of the hydrogen-ionizing radiation (or ionization parameter) and not the hardness of the ionizing radiation field.

We cannot directly measure the hardness of the UV field from our data, but as was shown by Levesque et al. (2010) and Khramtsova et al. (2014; see also Figure 5 in Appendix A),

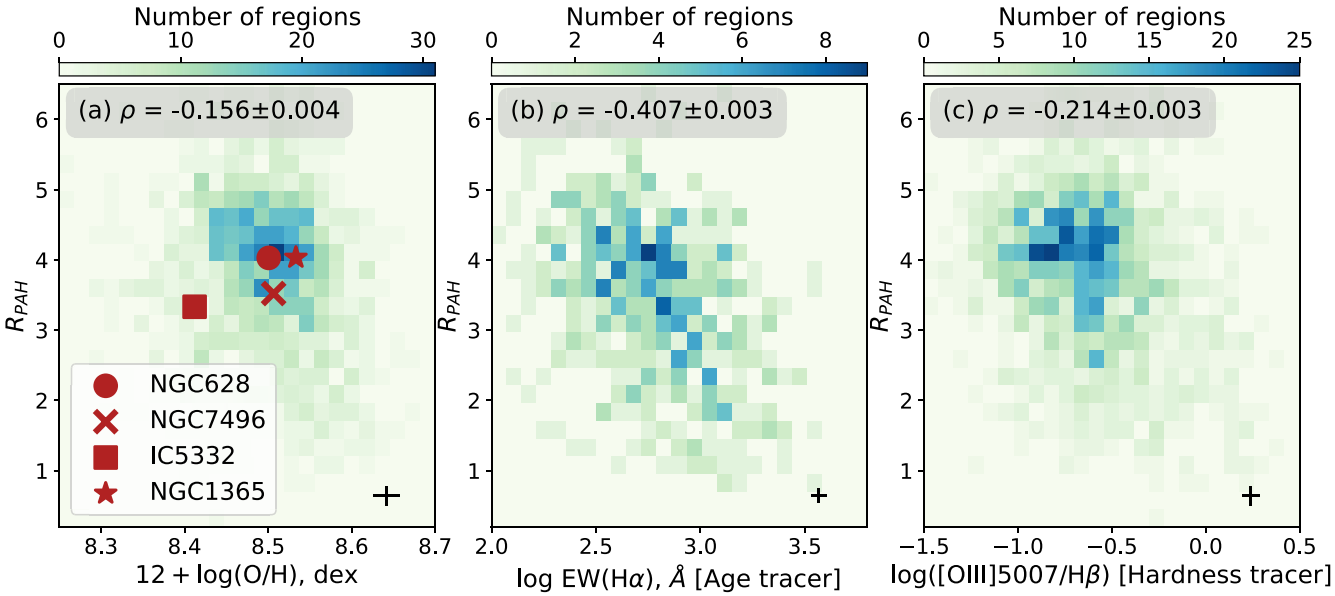

Figure 4. Correlation of the PAH fraction, traced by $R_{\rm PAH}$, with different physical conditions. Panel (a): correlation with oxygen abundance, $12 + \log({\rm O/H})$, with red symbols showing the mean value for each galaxy. Panel (b): equivalent width of Hα, EW(Hα), corrected for the contribution of the underlying old stellar population, and a tracer of H II region age. Note that because of the large uncertainty introduced by this background continuum subtraction, we consider here only regions with relative error $\delta({\rm EW(H}\alpha)) < 10\%$. Panel (c): $\log([{\rm O\,III}]/{\rm H}\beta)$, a tracer of the hardness of the UV radiation. Spearman's correlation coefficient (ρ) is given in the corner of each plot. Its uncertainty is derived in the same way as in Figure 2. The error bars in the right-hand corner correspond to the 95th percentile uncertainties of the measured values.

[O III]/Hβ is a reasonable tracer of UV hardness at fixed metallicity. This ratio also depends on the ionization parameter but to a lesser extent than [S III]/[S II]. Given this, we would expect to see a strong correlation between $R_{\rm PAH}$ and [O III]/Hβ if the PAH destruction in H II regions is regulated mostly by the hardness of the ionizing radiation field and not by its intensity. In fact, we see only a relatively weak correlation between these parameters in Figure 4(c). Note that our result remains unchanged if we exclude IC 5332 from consideration (and only focus on the three galaxies of approximately similar metallicity). Thus, it is probable that it is indeed the ionization parameter, and not hardness, that drives the correlation in Figure 2.

4.4. Toward an Evolutionary Sequence

The dependence of $R_{\rm PAH}$ on the ionization parameter can be viewed within the context of an H II region evolutionary sequence. We expect the ionization parameter to decrease with age, as older star clusters produce fewer ionizing photons and the H II region expands (Dopita et al. 2006). The equivalent width of the Balmer lines (e.g., EW(Hα)) is another (more common) indicator that decreases with the age of an H II region (Levesque & Leitherer 2013). In Figure 4(b), we identify a correlation between $R_{\rm PAH}$ and EW(Hα), where EW(Hα) has been corrected for the contribution of the underlying old stellar population.[34] The $R_{\rm PAH}$ decreases with EW(Hα); however, the correlation is not as prominent as the correlation with [S III]/[S II]. This suggests that the fraction of PAH molecules in the total dust mass increases slightly with time, if we assume that EW(Hα) is a good tracer of the age of the H II region. Note that we do not find a secondary correlation between the residuals $\Delta R_{\rm PAH}$ (obtained after subtraction of the relation defined by Equation (2) from the observed data) on EW(Hα) (Figure 3(d)), probably because both EW(Hα) and [S III]/[S II] should decrease with the age. If such correlation with age is real, then it implies that the PAH fraction is higher in older regions. This can be explained if we assume that the balance between PAH formation and destruction changes with time. For example, the relative fraction of PAHs can increase with time if the very small grains have been destroyed or cleared from the older H II regions more efficiently than PAHs, or if PAHs (even gradually) build up as result of the destruction of larger dust grains (e.g., as a result of shattering).

Previous studies have revealed a possible evolution of the PAH abundance with the age of star-forming regions, but the behavior is quite complex and depends on the balance between the processes of formation and destruction of the dust grains and PAHs (e.g., Khramtsova et al. 2014; Wiebe et al. 2014; Lin et al. 2020). In particular, according to Khramtsova et al. (2014), $R_{\rm PAH}$ increases with age for low-metallicity regions, and this trend flattens for higher metallicities. The correlation of $R_{\rm PAH}$ with EW(Hα) in Figure 4(b) is relatively weak, and EW(Hα) itself is not always a strong tracer of H II region age (Scheuermann et al. 2023); thus, we are hesitant to interpret this trend as strong evidence for an age sequence. Future work linking H II regions with age dating of ionizing stellar clusters using PHANGS–HST and PHANGS–JWST data will provide a more robust quantification of these tentative age trends (see also Dale et al. 2023).

4.5. The Role of Shocks

Beyond the correlations identified in this letter, we searched for other properties regulating the PAH fraction on the scales of individual H II regions. In particular, we tested whether shocks affect the PAH fraction by considering regions associated with high Hα velocity dispersion (O. V. Egorov et al. 2023, in preparation) or classified as shock ionized by diagnostic optical

[34] This correction is performed by subtracting the corresponding continuum derived in a circular aperture surrounding each H II region. For details, see Scheuermann et al. (2023).

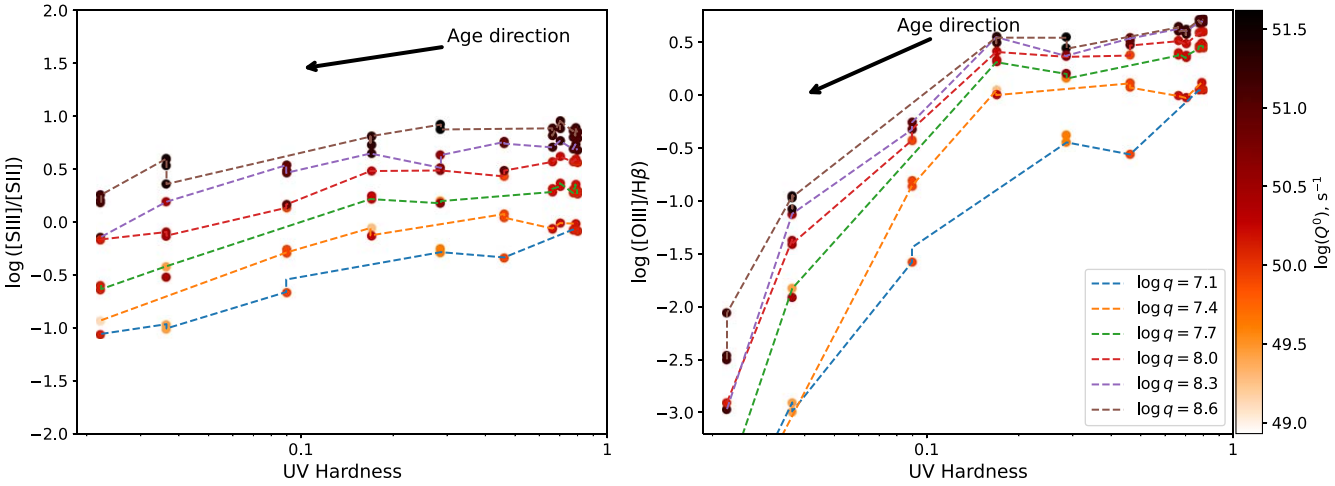

Figure 5. Dependence of [S III]/[S II] (left panel) and [O III]/Hβ (right panel) optical emission line ratios on the hardness of the ionizing UV radiation and the ionization parameter q, according to a grid of STARBURST99 and CLOUDY models (see text). Different points are the individual nodes of the model grid, defined by the different mass and age of the ionizing cluster and the density of the H II region. The color of the points encodes the number of hydrogen-ionizing photons, Q^0.

emission line ratios (Congiu et al. 2023) but did not find any significant differences from the trends we identify using the H II regions in Figure 2. Thus, the ionization parameter (intensity of hydrogen-ionizing radiation) appears to be the dominant factor in defining the mechanisms for PAH destruction in H II regions.

5. Summary

With JWST, it is now possible to systematically study the properties of the PAH component of the ISM at the scales of individual H II regions in the galaxies beyond our Local Group, building a more representative picture of the interplay between ionizing sources and dust properties. As a pilot study, we analyze the PAH fraction in 1529 H II regions within the disks of four nearby star-forming galaxies from the PHANGS–JWST program and compare them with the properties of the ionized gas as obtained from PHANGS–MUSE observations. We find a strong anticorrelation between PAH fraction and ionization parameter, with a steeper dependence for more luminous regions. This is consistent with a scenario where the destruction of the PAH molecules is set by the hydrogen-ionizing UV radiation, though it is not clear if the observed trend reflects an evolutionary sequence. We find only a weak secondary dependence between PAH fraction and oxygen abundance, although we note that we cover a very limited range ($\sim$0.3 dex) in metallicity in our sample. Together with the results presented in Chastenet et al. (2023a), this implies that, in contrast to the diffuse ISM, the metallicity becomes unimportant in defining the balance between PAH formation and destruction in H II regions, where the presence of ionized gas and hard radiation dominate.

In this study leveraging new JWST observations for four star-forming galaxies, we have demonstrated that hydrogen-ionizing UV radiation is the dominant mechanism for PAH destruction in H II regions.

This work is based on observations made with the NASA/ESA/CSA JWST. The data were obtained from the Mikulski Archive for Space Telescopes at the Space Telescope Science Institute, which is operated by the Association of Universities for Research in Astronomy, Inc., under NASA contract NAS 5-03127. The observations are associated with JWST program 2107. The specific observations analyzed can be accessed via 10.17909/9bdf-jn24. Based on observations collected at the European Southern Observatory under ESO programs 094.C-0623 (PI: Kreckel), 095.C-0473, 098.C-0484 (PI: Blanc), and 1100.B-0651 (PHANGS–MUSE; PI: Schinnerer), as well as 094.B-0321 (MAGNUM; PI: Marconi), 099.B-0242, 0100.B-0116, 098.B-0551 (MAD; PI: Carollo), and 097.B-0640 (TIMER; PI: Gadotti).

K.K., O.E., and F.S. gratefully acknowledge funding from the Deutsche Forschungsgemeinschaft (DFG, German Research Foundation) in the form of an Emmy Noether Research Group (grant No. KR4598/2-1; PI: Kreckel). E.J.W., R.S.K., and S.C.O.G. acknowledge funding from the Deutsche Forschungsgemeinschaft (DFG, German Research Foundation) project ID 138713538—SFB 881 ("The Milky Way System," subprojects A1, B1, B2, B8, P1). H.A.P. acknowledges support by the National Science and Technology Council of Taiwan under grant 110-2112-M-032-020-MY3. T.G.W. and E.S. acknowledge funding from the European Research Council (ERC) under the European Union's Horizon 2020 research and innovation program (grant agreement No. 694343). M.B. acknowledges support from FONDECYT regular grant 1211000 and by ANID BASAL project FB210003. J.M.D.K. gratefully acknowledges funding from the European Research Council (ERC) under the European Union's Horizon 2020 research and innovation program via the ERC Starting Grant MUSTANG (grant agreement No. 714907). COOL Research DAO is a Decentralized Autonomous Organization supporting research in astrophysics aimed at uncovering our cosmic origins. E.C. acknowledges support from ANID Basal projects ACE210002 and FB210003. F.B. would like to acknowledge funding from the European Research Council (ERC) under the European Union's Horizon 2020 research and innovation program (grant agreement No. 726384/Empire). M.C. gratefully acknowledges funding from the DFG through an Emmy Noether Research Group (grant No. CH2137/1-1). R.S.K. and S.C.O.G. acknowledge support from the European Research Council via the ERC Synergy Grant "ECOGAL" (project ID 855130), the Heidelberg Cluster of Excellence (EXC 2181-390900948) "STRUCTURES," funded by the German Excellence Strategy, and the German Ministry for Economic Affairs

and Climate Action for funding in project "MAINN" (funding ID 50OO2206). E.R. acknowledges the support of the Natural Sciences and Engineering Research Council of Canada (NSERC), funding reference No. RGPIN-2022-03499. K.G. is supported by the Australian Research Council through Discovery Early Career Researcher Award (DECRA) Fellowship DE220100766 funded by the Australian Government. K. G. is supported by the Australian Research Council Centre of Excellence for All Sky Astrophysics in 3 Dimensions (ASTRO 3D) through project No. CE170100013. G.A.B. acknowledges the support from ANID Basal project FB210003. J.C. acknowledges support from ERC starting grant No. 851622 DustOrigin. A.K.L. gratefully acknowledges support by grants 1653300 and 2205628 from the National Science Foundation, award JWST-GO-02107.009-A, and a Humboldt Research Award from the Alexander von Humboldt Foundation. J.P. acknowledges support by DAOISM grant ANR-21-CE31-0010 and the Programme National "Physique et Chimie du Milieu Interstellaire" (PCMI) of CNRS/INSU with INC/INP, cofunded by CEA and CNES.

Facilities: JWST(MIRI), VLT(MUSE).

Software: Astropy (Astropy Collaboration et al. 2013, 2018), Cloudy (Ferland et al. 2017), pyCloudy (Morisset 2013), Starburst99 (Leitherer et al. 1999, 2014), WebbPSF (Perrin et al. 2014).

Appendix A
Physical Interpretation of Emission Line Ratios in the Context of Photoionization Modeling

Here we consider how the hardness and intensity of the ionizing radiation impact the [S III]/[S II] and [O III]/Hβ line ratios and how they evolve with the age of the H II regions. Kreckel et al. (2022) presented STARBURST99 (Leitherer et al. 1999, 2014) and CLOUDY (Ferland et al. 2017) models computed for a grid of star clusters and H II region physical properties matched to the observed properties as derived in the PHANGS–MUSE and PHANGS–HST data. Here we use a subset of their models for metallicity $Z \sim 0.6\ Z_{\odot}$ (approximately equal to the metallicity of the four galaxies considered in this work; see Table 1). We consider clusters of mass $\log(M_{*}/M_{\odot}) = 3.5$, 4.5, 5.5 and age $t = 1$, ..., 9 Myr (with a step of 1 Myr) as the ionizing source of a cloud with constant hydrogen density $n_{\rm H} \simeq n_{\rm e} = 20$, 90, and 300 cm^{-3}. For simplicity, here we consider only one nebular geometry: a shell with an inner radius of 15 pc and filling factor ff = 1.

Similar to Khramtsova et al. (2014), we parameterize the hardness of the UV radiation as the ratio of the total flux in the ionizing continuum at short wavelengths (20–912 Å) to that at longer wavelengths (912–2000 Å). Figure 5 shows how both ionization parameter and UV hardness are traced by the emission line ratios [S III]/[S II] and [O III]/Hβ. These line ratios are sensitive to both parameters, but [S III]/[S II] shows a stronger dependence on the ionization parameter, while [O III]/Hβ is less sensitive to the ionization parameter but varies significantly with the hardness of the UV radiation. Thus, by analyzing the dependence of the PAH fraction in H II regions using both of these line ratios, we can disentangle whether UV hardness or the number of ionizing photons (proportional to the ionization parameter) is the main driver for PAH destruction. We consider this in Section 4.3.

Appendix B
Testing the Impact of Limited Angular Resolution and Contamination by Emission from the Diffuse ISM

As we show in Section 4.1, a large fraction of the H II regions analyzed in this paper are not well resolved by our PHANGS–MUSE observations ($R/\mathrm{PSF} < 1$ in Figure 2(d)). Also, we do not correct the measured fluxes of the optical emission lines and mid-IR bands for a local background, as implementing such subtraction is a fairly uncertain process. Nevertheless, both of these factors may affect our measurements. In order to check that our conclusions are not biased because of these factors, we perform several tests in this section.

In unresolved H II regions, the measured value of $R_{\rm PAH}$ may be biased because of a larger contribution from the surrounding PDR and diffuse ISM to the aperture, which is indeed seen in Figure 2(d). In Figure 6, we repeat the analysis presented in Section 4.1 but consider only the resolved H II regions having $R/\mathrm{PSF} > 1$ (44% of the total number of H II regions in the analysis). As shown, the relations drawn from the entire sample are the same (but tighter) as the relations observed for the resolved H II regions alone.

The second test shown in Figure 7 allows us to confirm that the contamination by the diffuse ISM does not introduce a bias to our results. Here we follow the same approach as in Kreckel et al. (2022); we consider only the H II regions with a significant contrast in the Hα and [S II] fluxes and the mid-IR bands compared to the local background. We estimate the contrast as the maximal value of $C = F_{\rm HII}/(I_{\rm bgr} \times S)$ among all considered lines/bands, where $F_{\rm H\,II}$ is a measured integral flux of the H II region, $I_{\rm bgr}$ is the median brightness of the surrounding local background estimated across a 10″ circular aperture after masking all H II regions, and S is the area within the H II region mask. In Figure 7, we show only regions with a contrast $C > 2$, for which the contribution of the diffuse emission to the total flux is negligible (∼29% of the entire sample). This "clear" sample demonstrates the same trends as the entire sample in Figure 2.

We may thus conclude that the presence of unresolved H II regions and contamination by the diffuse ISM (which is still unavoidable for galaxies outside the Local Group) does not affect the results of our analysis but adds scatter to the observed relations. Note, however, that when considering these subsamples, we cannot judge how reliable our findings are regarding the secondary dependence of the PAH fraction on metallicity (Section 4.2, Figure 3) because the number of regions at the low-metallicity end of the "clear" samples analyzed is too small.

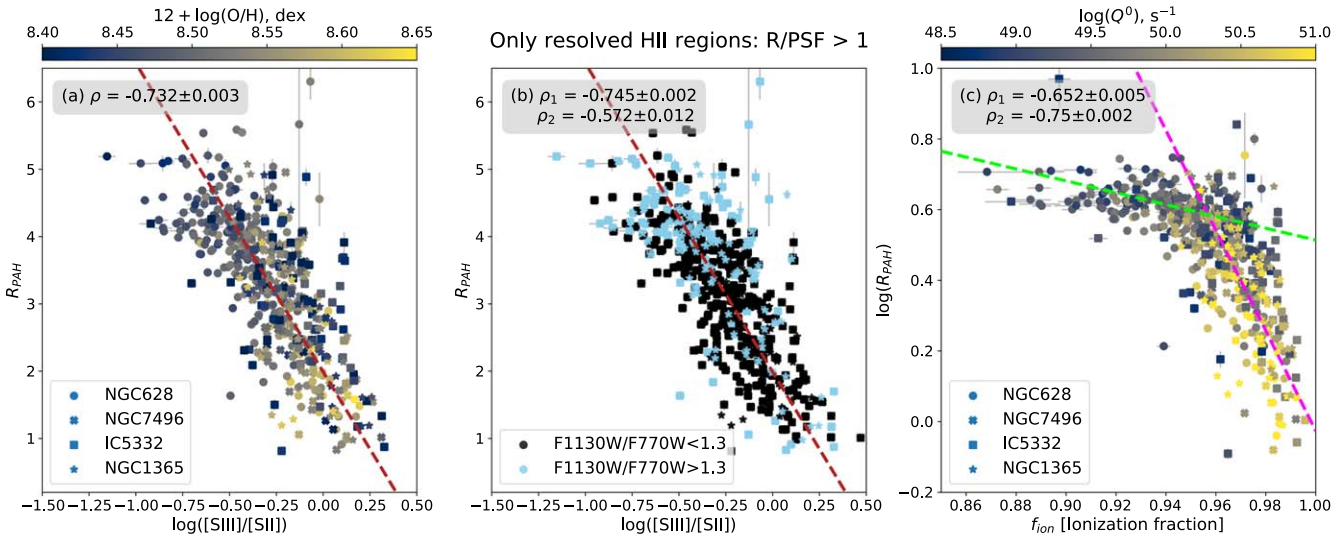

Figure 6. Same as Figures 2(a)–(c) but for the resolved H II regions only (those with $R/\mathrm{PSF} > 1$ in Figure 2(d)). The colored lines show the same linear regressions as in Figure 2.

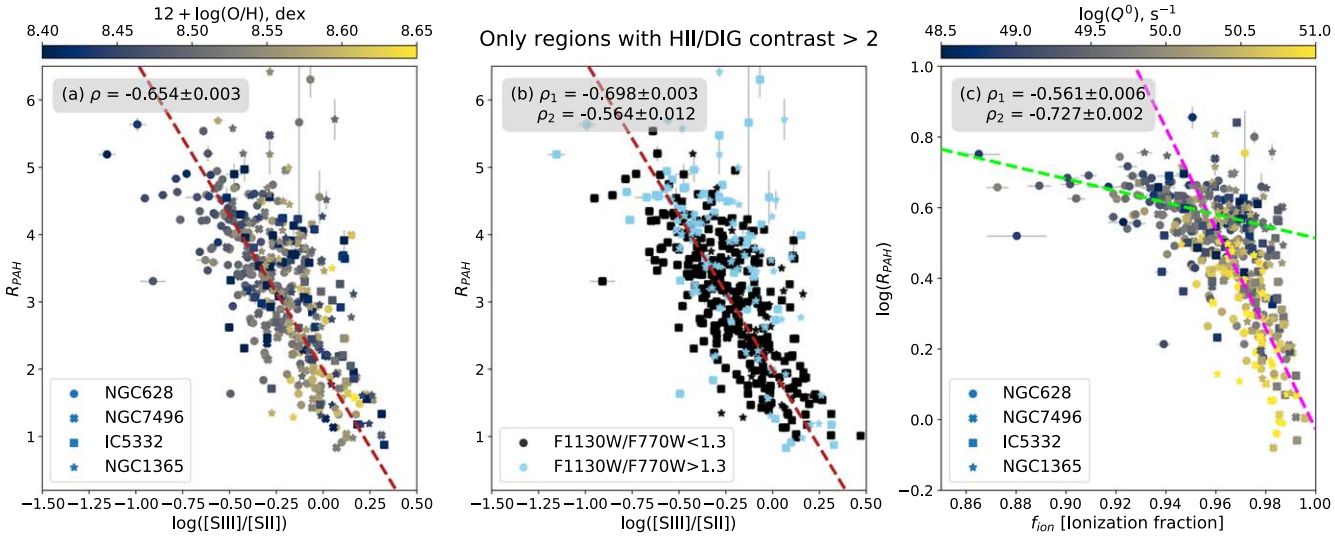

Figure 7. Same as Figure 6 but for a subsample of the H II regions with a large contrast against the surrounding local background in the Hα, [S II] emission lines, and mid-IR bands.

ORCID iDs

Oleg V. Egorov https://orcid.org/0000-0002-4755-118X
Kathryn Kreckel https://orcid.org/0000-0001-6551-3091
Karin M. Sandstrom https://orcid.org/0000-0002-4378-8534
Adam K. Leroy https://orcid.org/0000-0002-2545-1700
Simon C. O. Glover https://orcid.org/0000-0001-6708-1317
Brent Groves https://orcid.org/0000-0002-9768-0246
J. M. Diederik Kruijssen https://orcid.org/0000-0002-8804-0212
Ashley. T. Barnes https://orcid.org/0000-0003-0410-4504
Francesco Belfiore https://orcid.org/0000-0002-2545-5752
F. Bigiel https://orcid.org/0000-0003-0166-9745
Guillermo A. Blanc https://orcid.org/0000-0003-4218-3944
Médéric Boquien https://orcid.org/0000-0003-0946-6176
Yixian Cao https://orcid.org/0000-0001-5301-1326
Jérémy Chastenet https://orcid.org/0000-0002-5235-5589
Mélanie Chevance https://orcid.org/0000-0002-5635-5180
Enrico Congiu https://orcid.org/0000-0002-8549-4083
Daniel A. Dale https://orcid.org/0000-0002-5782-9093
Eric Emsellem https://orcid.org/0000-0002-6155-7166
Kathryn Grasha https://orcid.org/0000-0002-3247-5321
Ralf S. Klessen https://orcid.org/0000-0002-0560-3172
Kirsten L. Larson https://orcid.org/0000-0003-3917-6460
Daizhong Liu https://orcid.org/0000-0001-9773-7479
Eric J. Murphy https://orcid.org/0000-0001-7089-7325
Hsi-An Pan https://orcid.org/0000-0002-1370-6964
Ismael Pessa https://orcid.org/0000-0002-0873-5744
Jérôme Pety https://orcid.org/0000-0003-3061-6546
Erik Rosolowsky https://orcid.org/0000-0002-5204-2259
Fabian Scheuermann https://orcid.org/0000-0003-2707-4678
Eva Schinnerer https://orcid.org/0000-0002-3933-7677
Jessica Sutter https://orcid.org/0000-0002-9183-8102
David A. Thilker https://orcid.org/0000-0002-8528-7340

Elizabeth J. Watkins https://orcid.org/0000-0002-7365-5791
Thomas G. Williams https://orcid.org/0000-0002-0012-2142

References

Allain, T., Leach, S., & Sedlmayr, E. 1996, A&A, 305, 602
Anand, G. S., Lee, J. C., Van Dyk, S. D., et al. 2021a, MNRAS, 501, 3621
Anand, G. S., Rizzi, L., Tully, R. B., et al. 2021b, AJ, 162, 80
Anderson, L. D., Bania, T. M., Balser, D. S., et al. 2014, ApJS, 212, 1
Aniano, G., Draine, B. T., Gordon, K. D., & Sandstrom, K. 2011, PASP, 123, 1218
Aniano, G., Draine, B. T., Hunt, L. K., et al. 2020, ApJ, 889, 150
Astropy Collaboration, Price-Whelan, A. M., Sipőcz, B. M., et al. 2018, AJ, 156, 123
Astropy Collaboration, Robitaille, T. P., Tollerud, E. J., et al. 2013, A&A, 558, A33
Bacon, R., Accardo, M., Adjali, L., et al. 2010, Proc. SPIE, 7735, 773508
Baldwin, J. A., Phillips, M. M., & Terlevich, R. 1981, PASP, 93, 5
Belfiore, F., Santoro, F., Groves, B., et al. 2022, A&A, 659, A26
Binder, B. A., & Povich, M. S. 2018, ApJ, 864, 136
Bocchio, M., Micelotta, E. R., Gautier, A.-L., & Jones, A. P. 2012, A&A, 545, A124
Bolatto, A. D., Simon, J. D., Stanimirovic, S., et al. 2007, ApJ, 655, 212
Burkhardt, A. M., Long Kelvin Lee, K., Bryan Changala, P., et al. 2021, ApJL, 913, L18
Calzetti, D. 2013, in Secular Evolution of Galaxies, ed. J. Falcón-Barroso & J. H. Knapen (Cambridge: Cambridge Univ. Press), 419
Chastenet, J., Bot, C., Gordon, K. D., et al. 2017, A&A, 601, A55
Chastenet, J., Sandstrom, K., Chiang, I.-D., et al. 2019, ApJ, 876, 62
Chastenet, J., Sutter, J., Sandstrom, K. M., et al. 2023a, ApJL, 944, L11
Chastenet, J., Sutter, J., Sandstrom, K. M., et al. 2023b, ApJL, 944, L12
Cherchneff, I., Barker, J. R., & Tielens, A. G. G. M. 1992, ApJ, 401, 269
Congiu, E., Blanc, G. A., Belfiore, F., et al. 2023, A&A, submitted
Dale, D. A., Boquien, M., Barnes, A. T., et al. 2023, ApJL, 944, L23
Dopita, M. A., Fischera, J., Sutherland, R. S., et al. 2006, ApJ, 647, 244
Draine, B. T. 2011, ApJ, 732, 100
Draine, B. T., & Li, A. 2001, ApJ, 551, 807
Draine, B. T., & Li, A. 2007, ApJ, 657, 810
Draine, B. T., Li, A., Hensley, B. S., et al. 2021, ApJ, 917, 3
Emsellem, E., Schinnerer, E., Santoro, F., et al. 2022, A&A, 659, A191
Engelbracht, C. W., Gordon, K. D., Rieke, G. H., et al. 2005, ApJL, 628, L29
Engelbracht, C. W., Rieke, G. H., Gordon, K. D., et al. 2008, ApJ, 678, 804
Everett, J. E., & Churchwell, E. 2010, ApJ, 713, 592
Ferland, G. J., Chatzikos, M., Guzmán, F., et al. 2017, RMxAA, 53, 385
Gail, H. P., & Sedlmayr, E. 1979, A&A, 77, 165
García-Bernete, I., Rigopoulou, D., Alonso-Herrero, A., et al. 2022, MNRAS, 509, 4256
Gordon, K. D., Engelbracht, C. W., Rieke, G. H., et al. 2008, ApJ, 682, 336
Groves, B., Dopita, M. A., Sutherland, R. S., et al. 2008, ApJS, 176, 438
Groves, B., Kreckel, K., Santoro, F., et al. 2023, MNRAS, arXiv:2301.03811
Hirashita, H., & Yan, H. 2009, MNRAS, 394, 1061
Hunt, L. K., Thuan, T. X., Izotov, Y. I., & Sauvage, M. 2010, ApJ, 712, 164
Jensen, J. J., Honig, S. F., Rakshit, S., et al. 2017, MNRAS, 470, 3071
Jones, A. P., Tielens, A. G. G. M., & Hollenbach, D. J. 1996, ApJ, 469, 740
Kewley, L. J., & Dopita, M. A. 2002, ApJS, 142, 35
Kewley, L. J., Nicholls, D. C., & Sutherland, R. S. 2019, ARA&A, 57, 511
Khramtsova, M. S., Wiebe, D. S., Boley, P. A., & Pavlyuchenkov, Y. 2013, MNRAS, 431, 2006
Khramtsova, M. S., Wiebe, D. S., Lozinskaya, T. A., & Egorov, O. V. 2014, MNRAS, 444, 757
Kourkchi, E., Courtois, H. M., Graziani, R., et al. 2020, AJ, 159, 67
Kreckel, K., Egorov, O. V., Belfiore, F., et al. 2022, A&A, 667, A16
Kumari, N., Amorin, R., Perez-Montero, E., Vilchez, J., & Maiolino, R. 2021, MNRAS, 508, 1084
Lai, T. S. Y., Armus, L., U, V., et al. 2022, ApJL, 941, L36
Latter, W. B. 1991, ApJ, 377, 187
Lebouteiller, V., Bernard-Salas, J., Whelan, D. G., et al. 2011, ApJ, 728, 45
Lee, J. C., Sandstrom, K. M., Leroy, A. K., et al. 2023, ApJL, 944, L17
Lee, J. C., Whitmore, B. C., Thilker, D. A., et al. 2022, ApJS, 258, 10
Leitherer, C., Ekstrom, S., Meynet, G., et al. 2014, ApJS, 212, 14
Leitherer, C., Schaerer, D., Goldader, J. D., et al. 1999, ApJS, 123, 3
Leroy, A. K., Schinnerer, E., Hughes, A., et al. 2021, ApJS, 257, 43
Levesque, E. M., Kewley, L. J., & Larson, K. L. 2010, AJ, 139, 712
Levesque, E. M., & Leitherer, C. 2013, ApJ, 779, 170
Li, A. 2020, NatAs, 4, 339
Lin, Z., Calzetti, D., Kong, X., et al. 2020, ApJ, 896, 16
Madden, S. C., Galliano, F., Jones, A. P., & Sauvage, M. 2006, A&A, 446, 877
Mallory, K., Calzetti, D., & Lin, Z. 2022, ApJ, 933, 156
Maragkoudakis, A., Ivkovich, N., Peeters, E., et al. 2018, MNRAS, 481, 5370
Matsuura, M., Barlow, M. J., Zijlstra, A. A., et al. 2009, MNRAS, 396, 918
Matsuura, M., Woods, P. M., & Owen, P. J. 2013, MNRAS, 429, 2527
Micelotta, E. R., Jones, A. P., & Tielens, A. G. G. M. 2010a, A&A, 510, A36
Micelotta, E. R., Jones, A. P., & Tielens, A. G. G. M. 2010b, A&A, 510, A37
Montillaud, J., Joblin, C., & Toublanc, D. 2013, A&A, 552, A15
Morisset, C. 2013, pyCloudy: Tools to manage astronomical Cloudy photoionization code, Astrophysics Source Code Library, ascl:1304.020
Oey, M. S., López-Hernández, J., Kellar, J. A., et al. 2017, ApJ, 844, 63
O'Halloran, B., Satyapal, S., & Dudik, R. P. 2006, ApJ, 641, 795
Osterbrock, D. E., & Ferland, G. J. 2006, Astrophysics of Gaseous Nebulae and Active Galactic Nuclei (2nd edn; Sausalito, CA: Univ. Science Books)
Paladini, R., Umana, G., Veneziani, M., et al. 2012, ApJ, 760, 149
Paturel, G., Petit, C., Prugniel, P., et al. 2003, A&A, 412, 45
Pavlyuchenkov, Y., Kirsanova, M. S., & Wiebe, D. S. 2013, ARep, 57, 573
Perrin, M. D., Sivaramakrishnan, A., Lajoie, C.-P., et al. 2014, Proc. SPIE, 9143, 91433X
Pilyugin, L. S., & Grebel, E. K. 2016, MNRAS, 457, 3678
Povich, M. S., Stone, J. M., Churchwell, E., et al. 2007, ApJ, 660, 346
Querejeta, M., Schinnerer, E., Meidt, S., et al. 2021, A&A, 656, A133
Sandstrom, K., Koch, E. W., Leroy, A. K., et al. 2023, ApJL, 944, L8
Sandstrom, K. M., Bolatto, A. D., Draine, B. T., Bot, C., & Stanimirovic, S. 2010, ApJ, 715, 701
Santoro, F., Kreckel, K., Belfiore, F., et al. 2022, A&A, 658, A188
Seok, J. Y., Hirashita, H., & Asano, R. S. 2014, MNRAS, 439, 2186
Shaya, E. J., Tully, R. B., Hoffman, Y., & Pomarede, D. 2017, ApJ, 850, 207
Scheuermann, F., Kreckel, K., Barnes, A., et al. 2023, MNRAS, submitted
Smith, J. D. T., Draine, B. T., Dale, D. A., et al. 2007, ApJ, 656, 770
Thilker, D. A., Braun, R., & Walterbos, R. A. M. 2000, AJ, 120, 3070
Tielens, A. G. G. M. 2008, ARA&A, 46, 289
Whitcomb, C. M., Sandstrom, K., Murphy, E. J., & Linden, S. 2020, ApJ, 901, 47
Wiebe, D. S., Egorov, O. V., & Lozinskaya, T. A. 2011, ARep, 55, 585
Wiebe, D. S., Khramtsova, M. S., Egorov, O. V., & Lozinskaya, T. A. 2014, AstL, 40, 278
Wisnioski, E., Glazebrook, K., Blake, C., et al. 2012, MNRAS, 422, 3339